Large-scale manufacturing sulfide superionic conductor for advancing all-solid-state batteries

Wang, Shuo; Lou, Chenjie; Wu, Xinbin; Lin, Jing; Gautam, Ajay; Cheng, Zhu; Zhang, Shengnan; Strauss, Florian; Tang, Mingxue; Nan, Ce Wen

DOI
10.1016/j.matt.2025.102135

Publication date
2025

Document Version
Final published version

Published in
Matter

Citation (APA)
Wang, S., Lou, C., Wu, X., Lin, J., Gautam, A., Cheng, Z., Zhang, S., Strauss, F., Tang, M., Nan, C. W., & More Authors (2025). Large-scale manufacturing sulfide superionic conductor for advancing all-solid-state batteries. *Matter*, *8*(9), Article 102135. https://doi.org/10.1016/j.matt.2025.102135

Matter

Article

Large-scale manufacturing sulfide superionic conductor for advancing all-solid-state batteries

Graphical abstract

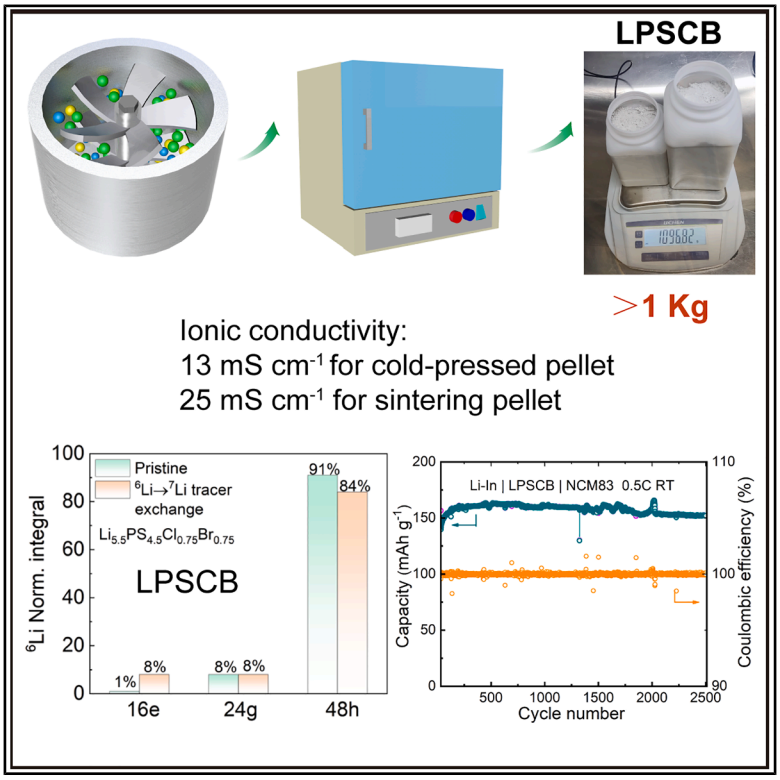

Highlights

- Large-scale production of over 1 kg per batch of lithium argyrodite is achieved
- The ion transport mechanism of the $Li_{5.5}PS_{4.5}Cl_{0.75}Br_{0.75}$ electrolyte is revealed
- Long-term stable cycling is achieved for the LPSCB-based all-solid-state battery

Authors

Shuo Wang, Chenjie Lou, Xinbin Wu, ..., Yang Shen, Yuanhua Lin, Ce-Wen Nan

Correspondence

shuowang@whut.edu.cn (S.W.), mxtang@ustb.edu.cn (M.T.), cwnan@mail.tsinghua.edu.cn (C.-W.N.)

In brief

Kilogram-scale stable synthesis of sulfide electrolytes was achieved through rapid dry mixing followed by heat treatment. Owing to enhanced intercage transport dynamics, the as-prepared Cl/Br dual-doped halogen-rich lithium argyrodites exhibit ultrahigh room temperature ionic conductivity (twice that of conventional liquid electrolytes). Benefiting from excellent interfacial stability, the assembled all-solid-state batteries demonstrate outstanding long-term cycling performance and rate performance.

Improvement
Enhanced performance with innovative design or material control

Wang et al., 2025, Matter 8, 102135
September 3, 2025
https://doi.org/10.1016/j.matt.2025.102135

CellPress

Please cite this article in press as: Wang et al., Large-scale manufacturing sulfide superionic conductor for advancing all-solid-state batteries, Matter (2025), https://doi.org/10.1016/j.matt.2025.102135

Matter

CellPress

Article

Large-scale manufacturing sulfide superionic conductor for advancing all-solid-state batteries

Shuo Wang,[1,6,7,*] Chenjie Lou,[2,6] Xinbin Wu,[3] Jing Lin,[4] Ajay Gautam,[5] Shenghao Li,[1] Jielei Huang,[1] Zhu Cheng,[5] Shengnan Zhang,[5] Xin Zhang,[1] Florian Strauss,[4] Torsten Brezesinski,[4] Guoqiang Luo,[1] Mingxue Tang,[2,*] Yang Shen,[3] Yuanhua Lin,[3] and Ce-Wen Nan[3,*]

[1]Center of Smart Materials and Devices, State Key Laboratory of Advanced Technology for Materials Synthesis and Processing, School of Material Science and Engineering, Wuhan University of Technology, Wuhan 430070, China

[2]Center for High Pressure Science and Technology Advanced Research, Beijing 100094, China

[3]State Key Laboratory of New Ceramics and Fine Processing, School of Materials Science and Engineering, Tsinghua University, Beijing 100084, China

[4]Institute of Nanotechnology, Karlsruhe Institute of Technology (KIT), Kaiserstr. 12, 76131 Karlsruhe, Germany

[5]Department of Radiation Science and Technology, Delft University of Technology, 2629 JB Delft, the Netherlands

[6]These authors contributed equally

[7]Lead contact

*Correspondence: shuowang@whut.edu.cn (S.W.), mxtang@ustb.edu.cn (M.T.), cwnan@mail.tsinghua.edu.cn (C.-W.N.)

https://doi.org/10.1016/j.matt.2025.102135

PROGRESS AND POTENTIAL Lithium argyrodites, due to their high room temperature ionic conductivities and ease of processing, are favorable solid electrolytes (SEs) for all-solid-state batteries. However, the low preparation efficiency and poor cycling performance arising from continuous side reactions at the SEI electrode interface hinder their large-scale applications in solid-state batteries. Herein, we successfully achieve large-scale production (over 1 kg per batch in the lab for the first time) of $Li_{5.5}PS_{4.5}Cl_{0.75}Br_{0.75}$ (LPSCB) by fast dry mixing followed by annealing, which presents high room temperature ionic conductivities of 13 mS cm^{-1} for cold-pressed and 25 mS cm^{-1} for sintered pellets, along with a low activation energy of 0.24 eV. Combining neutron powder diffraction and $^{6}Li \rightarrow {}^{7}Li$ tracer-exchange nuclear magnetic resonance (NMR) spectroscopy measurements, the origin of fast Li^{+} migration in the material is revealed. A significant quantity of the intercage jumps occurs through the 48*h*-16*e*-48*h* pathway, enabling faster ion conduction in LPSCB. The assembled cells using LPSCB and a Li_3BO_3-coated single-crystal $LiNi_{0.83}Co_{0.11}Mn_{0.06}O_2$ can be cycled for over 2,500 cycles at a 0.5 C rate and 1,800 cycles at a 2 C rate without any capacity degradation. Moreover, a high areal capacity of 2.8 mAh cm^{-2} is also achieved for the cell after 440 cycles. Our results provide new insights into the ion transport mechanism of superionic conductors and demonstrate that LPSCB is one of the most promising candidates for accelerating the commercialization of sulfide-based all-solid-state batteries.

SUMMARY

Lithium argyrodites with high ionic conductivities are favorable solid electrolytes (SEs) for all-solid-state batteries (ASSBs). However, their low preparation efficiency and poor cycling performance hinder their large-scale applications. In this work, we demonstrate successful large-scale production (over 1 kg per batch for the first time) of $Li_{5.5}PS_{4.5}Cl_{0.75}Br_{0.75}$ (LPSCB) by fast dry mixing followed by annealing, which presents high room temperature ionic conductivities of 13 mS cm^{-1} for cold-pressed and 25 mS cm^{-1} for sintered pellets. Combining neutron powder diffraction and $^{6}Li \rightarrow {}^{7}Li$ tracer-exchange nuclear magnetic resonance (NMR) spectroscopy measurements, we show that intercage jumps frequently occur through the 48*h*-16*e*-48*h* pathway in LPSCB, promoting the overall lithium conduction. The assembled ASSBs using LPSCB and a $LiNi_{0.83}Co_{0.11}Mn_{0.06}O_2$ electrode can be cycled for over 2,500 cycles at a 0.5 C rate and 1,800 cycles at a 2 C rate without any capacity degradation. Our results will accelerate the commercialization of sulfide SE for ASSBs.

Please cite this article in press as: Wang et al., Large-scale manufacturing sulfide superionic conductor for advancing all-solid-state batteries, Matter (2025), https://doi.org/10.1016/j.matt.2025.102135

INTRODUCTION

All-solid-state batteries (ASSBs) implementing non-flammable, inorganic solid electrolytes (SEs) have emerged as one of the promising next-generation batteries, given their potential to achieve higher energy density and enhanced safety.[1–6] Developing highly ionically conductive SEs relying on low-cost precursors and possessing good electrochemical stability against oxide cathodes would facilitate the realization of high-performing ASSBs.[7–10] Inorganic SEs typically include oxides, sulfides, and halides.[11–14] Among them, sulfide electrolytes, especially lithium argyrodites, have received extensive attention owing to their high room temperature ionic conductivity, low cost, good ductility, and high kinetic stability toward the electrodes.[15–17] The most prevalent lithium argyrodites are Li_6PS_5X (X = Cl and Br), reaching ionic conductivities of 1–4 mS cm^{-1}.[15,18] An increase in the disorder of the S^{2-}/X^- ions occupying the 4*a*/4*d* sites in Li_6PS_5X will change the lithium substructure, thereby enhancing ionic conductivity. Theoretical calculations indicate that when Cl^- occupies 75% of the 4*d* site, the ionic conductivity of Li_6PS_5Cl is the highest.[19] In contrast, Li_6PS_5I exhibits a low ionic conductivity of about 0.001 mS cm^{-1}, which is primarily attributed to the absence of S^{2-}/I^- disorder.[20] The aliovalent substitution of phosphorus with elements such as Ge or Si results in an increase of site inversion, altering the lithium substructure and thereby significantly improving ionic conductivity, e.g., in $Li_{6.6}P_{0.4}Ge_{0.6}S_5I$ (5.4 mS cm^{-1})[21] or $Li_{6.6}Si_{0.6}Sb_{0.4}S_5I$ (14.8 mS cm^{-1}).[22] It is notable that the ionic conductivity of $Li_{6.6}Si_{0.6}Sb_{0.4}S_5I$ rivals that of the well-known $Li_{10}GeP_2S_{12}$ (12 mS cm^{-1}).[23] However, Ge and Sb are relatively costly, and lithium argyrodites containing Ge, Si, or Sb are unstable toward the lithium-metal anode and high-voltage oxide cathodes, which would result in continuous degradation reactions, ultimately leading to cell failure.[24–26]

Substituting S with an excess of X in Li_6PS_5X to obtain halogen-rich lithium argyrodites is another effective method for improving ionic conductivity by increasing the degree of site inversion and generating additional Li^+ vacancies. Literature reports indicate that the room temperature ionic conductivity of $Li_{6-x}PS_{5-x}Cl_{1+x}$ ($0.5 \leq x \leq 0.7$) can be as high as 9–10 mS cm^{-1},[16,27] while for $Li_{5.5}P_{4.5}Br_{1.5}$, values of up to 5 mS cm^{-1} have been reported.[28] Recently, dual halogen doping of lithium argyrodites to obtain high-entropy ionic conductors has been proposed, aiming at further enhancing ionic conductivity.[29,30] Previous studies indicate that Li^+ ions mainly occupy 24*g* and 48*h* sites, and Li^+ mainly achieves rapid intercage conduction through 48*h*-48*h* pathways, resulting in high ionic conductivity.[16,27,31] However, it is difficult to explain why the ionic conductivity of dual-doped halogen-rich lithium argyrodites is higher than that of the single-doped counterpart. The underlying mechanisms responsible for the high ionic conductivity of dual-doped halogen-rich lithium argyrodites are still elusive and need to be further revealed by more, deeper characterizations, such as $^6Li \rightarrow {}^7Li$ tracer-exchange nuclear magnetic resonance (NMR) spectroscopy measurements.

Aside from the ionic conductivity and the cost, the preparation efficiency and energy consumption during the synthesis of lithium argyrodites should be considered. Currently, one of the prevailing methods for synthesizing halogen-rich sulfide electrolytes is a one-step high-energy ball-milling route. However, the ionic conductivity of SEs prepared using this method is low.[32] To further enhance the conductivity, a subsequent heat treatment is usually conducted following the ball milling process, thereby improving crystallinity.[16,27,33] Although adopting this can help to achieve high room temperature ionic conductivities of 10 mS cm^{-1} or so, it is usually time consuming and energy intensive. Typically, more than 10 h of ball milling is required, and the batch uniformity is poor. The yield obtained via this way is often limited, ranging from a few to tens of grams. Liquid-phase synthesis is also a popular method for preparing lithium argyrodites, involving a precursor suspension in organic media, stirring, subsequent solvent evaporation, and final heat treatment. However, the liquid-phase process is also time consuming, and solvent volatilization could increase costs and cause environmental issues.[34,35] Consequently, it is necessary to develop a method to prepare highly conductive sulfide SEs on the kilogram scale and with high batch consistency, which plays a vital role in facilitating the commercialization of ASSBs.

Despite the fact that the ionic conductivity of some sulfide electrolyte systems could reach 10 mS cm^{-1}, there are few reports that the capacity retention of ASSBs is higher than 90% after 1,000 cycles, which is mainly due to the chemo-mechanical failure inside the composite cathode.[36–38] In addition, to prepare a coating on the surface of the cathode active materials (CAMs), improving the electrochemical stability of the sulfide electrolytes could also enhance the cycling stability of the ASSBs.[25,37] By subtly controlling the Cl element content in the $Li_{6-x}PS_{5-x}Cl_{1+x}$ ($0 \leq x \leq 0.7$) electrolyte, the interfacial stability of the halogen-rich sulfide electrolytes against the high-voltage cathodes and the lithium metal anode can be significantly improved.[36,39] However, there is still a lack of detailed evaluation on the electrochemical stability of dual-doped halogen-rich electrolytes against high-voltage cathodes.

In this study, we use rapid dry mixing followed by heat treatment to prepare lithium argyrodites of a 1 kg batch size for the first time. The obtained $Li_{5.5}PS_{4.5}Cl_{0.75}Br_{0.75}$ (LPSCB) exhibits a high room temperature ionic conductivity of 13 mS cm^{-1} in the cold-pressed state and the lowest activation energy of 0.24 eV. Further hot pressing results in an ionic conductivity of 25 mS cm^{-1}, representing one of the highest values reported to date. The underlying mechanism of the enhanced ionic conductivity is examined via neutron powder diffraction (NPD), magic-angle spinning NMR (MAS NMR) spectroscopy, and $^6Li \rightarrow {}^7Li$ tracer-exchange NMR spectroscopy. Moreover, ASSBs employing a single-crystal $LiNi_{0.83}Co_{0.11}Mn_{0.06}O_2$@$Li_3BO_3$ (s-NCM83) cathode material, the as-prepared LPSCB, and an In/InLi anode are shown to deliver high areal capacities and exhibit high capacity retentions at various C rates. Electrochemical impedance spectroscopy (EIS) and X-ray photoelectron spectroscopy (XPS) measurements before and after cycling confirm that the interface between s-NCM83 and LPSCB (or $Li_{5.5}PS_{4.5}Cl_{1.5}$) is indeed kinetically stable.

RESULTS AND DISCUSSION

To successfully commercialize SEs, not only is a high room temperature ionic conductivity required, but also simple preparation

Please cite this article in press as: Wang et al., Large-scale manufacturing sulfide superionic conductor for advancing all-solid-state batteries, Matter (2025), https://doi.org/10.1016/j.matt.2025.102135

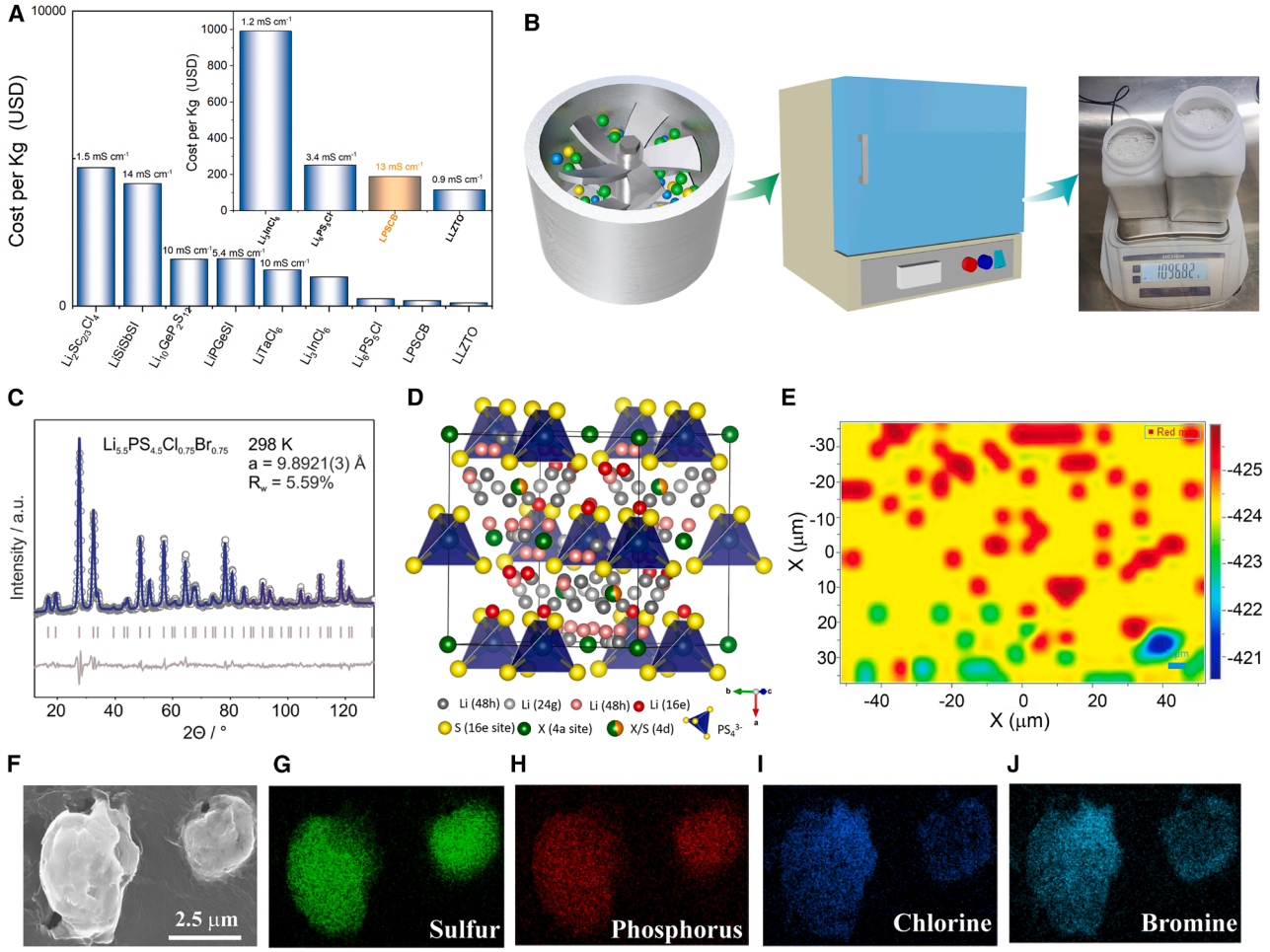

Figure 1. Schematic of the preparation process, structure characterization, and morphology of LPSCB electrolyte

(A) The total raw material costs and ionic conductivities of LPSCB and other oxide, sulfide, and halide SEs.

(B) Schematic representation of the synthesis of LPSCB, including fast dry mixing followed by annealing.

(C) Neutron powder diffraction (NPD) pattern of LPSCB with the corresponding Rietveld refinement profile. Dark gray circles represent the experimental data, the black line the calculated pattern, and the light gray line the difference profile. Vertical tick marks denote the position of expected Bragg reflections.

(D) Crystal structure of LPSCB, with the different Wyckoff positions and elements indicated in the legend below.

(E) Raman mapping image of an LPSCB pellet.

(F–J) SEM image of the LPSCB particles (F) and corresponding elemental maps for sulfur (G), phosphorus (H), chlorine (I), and bromine (J).

processes and low costs are required. Therefore, we have calculated and compared the total raw material costs of some typical sulfide, oxide, and halide SEs (Figure 1A).[15,21–23,40–43] The detailed cost calculation process is shown in Tables S1 and S2. Our designed LPSCB material presents one of the lowest costs and exhibits one of the highest ionic conductivities among the different inorganic SEs. A facile solid-state reaction method, including fast dry mixing followed by annealing, is adopted to synthesize the $Li_{5.5}PS_{4.5}Cl_{1.5}$, $Li_{5.3}PS_{4.3}Cl_{1.7}$, and LPSCB materials (Figure 1B). Compared with high-energy ball milling followed by annealing (10 g per batch at most), fast dry mixing followed by annealing is a highly efficient and energy-saving method that allows preparing SEs with over 1 kg per batch. To the best of our knowledge, this is the first report on the manufacturing of sulfide SEs on the hundred-gram scale in the lab.

X-ray diffraction (XRD) was conducted to confirm the phase purity of the $Li_{5.5}PS_{4.5}Cl_{1.5}$, $Li_{5.3}PS_{4.3}Cl_{1.7}$, and LPSCB SEs. As shown in Figure S1, it can be observed that all the synthesized electrolytes exhibit main reflections that can be assigned to the argyrodite phase, except for $Li_{5.3}PS_{4.3}Cl_{1.7}$, revealing the presence of some minor LiCl impurities. NPD measurements were also conducted on the LPSCB sample to gain a better understanding of the crystal structure, especially the lithium substructure. Figure 1C shows the NPD pattern of LPSCB at 298 K and the corresponding Rietveld refinement profile. The pattern can be indexed in the $F\bar{4}3m$ space group with a refined lattice parameter $a = 9.8921(3)$ Å. Full structural information is given in Table S1. Figure 1D depicts the calculated crystal structure, where the "free" S^{2-}, Cl^{-}, and Br^{-} ions form a face-centered cubic sublattice at Wyckoff positions 4*a* and 4*d*. The additional S^{2-} ions

Please cite this article in press as: Wang et al., Large-scale manufacturing sulfide superionic conductor for advancing all-solid-state batteries, Matter (2025), https://doi.org/10.1016/j.matt.2025.102135

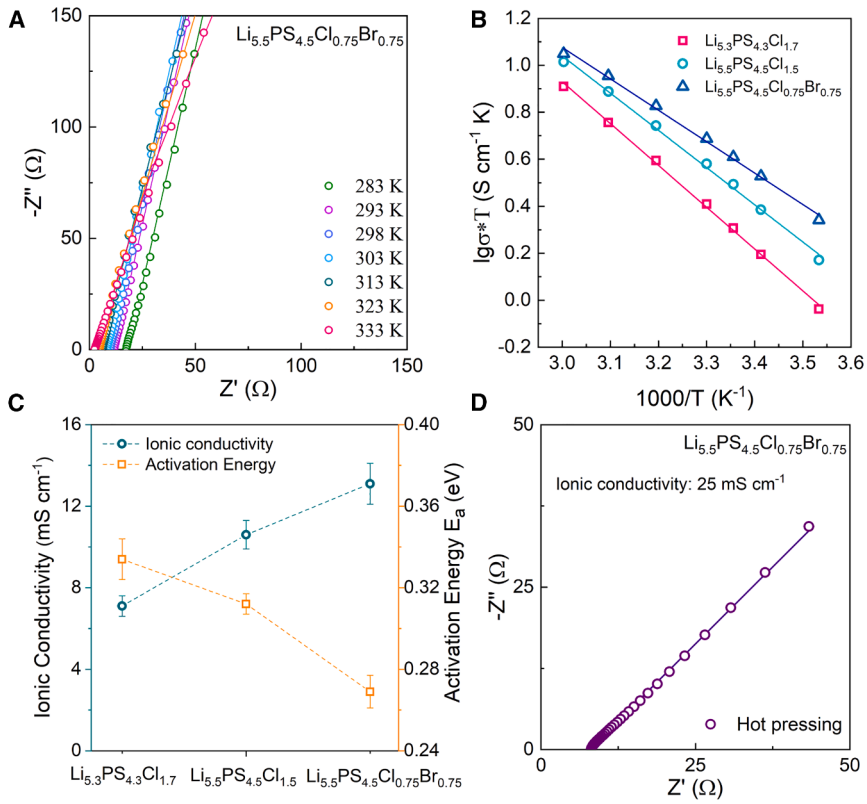

Figure 2. Ionic conductivity and activation energy of solid electrolytes

(A) Nyquist plots of LPSCB in the temperature range of 283–333 K.

(B and C) Arrhenius plots (B) and room temperature ionic conductivities and activation energies (C) for the $Li_{5.5}PS_{4.5}Cl_{1.5}$, $Li_{5.3}P_{4.3}Cl_{1.7}$, and LPSCB SEs.

(D) Nyquist plot of LPSCB after hot-pressing.

occupy the 16*e* Wyckoff site surrounding the P site (4*b*), thus creating PS_4^{3-} tetrahedra. Moreover, the lithium ions occupy two Wyckoff sites, including 24*g* and 48*h*. Additionally, the Cl^-/Br^- ions residing on the Wyckoff position 4*a* are usually mixed with S^{2-} ions at the 4*d* site, commonly denoted as S^{2-}/Cl^-/Br^- site inversion. The shared S^{2-}/Cl^-/Br^- occupancy on both the 4*a* and 4*d* sites was quantified via Rietveld analysis of the NPD data. On the 4*a* site, 18% S, 18% Cl, and 64% Br are found, while on the 4*d* site, 33% S, 57% Cl, and 11% Br are present (Table S3).

In addition, it can be observed in Figure S2 that the Raman spectra of 600 points in the scan range are similar. These peaks correspond to the PS_4^{3-} group from the $Li_{5.5}PS_{4.5}Cl_{1.5}$, $Li_{5.3}PS_{4.3}Cl_{1.7}$, and LPSCB SEs, and there is no peak related to the $P_2S_6^{4-}$ or $P_2S_7^{4-}$ group arising from impurities, indicating that the synthesized SEs are uniform without any impurities. In addition, it can also be seen from the Raman mapping (Figure 1E) that within the observation range of 100 × 70 μm^2, the main peaks are concentrated at 421–425 cm^{-1}, corresponding to the PS_4^{3-} group from the LPSCB. The main reason for the slight difference in color at different positions is that there are pits on the surface of the SE pellets, resulting in a slight shift in the peak position. The LPSCB particle morphology and elemental distribution were also probed using scanning electron microscopy (SEM) in combination with energy-dispersive X-ray (EDX) spectroscopy (Figures 1F–1J and S3). As shown, the particles have a size of several microns, with a homogeneous element distribution on a micrometer level.

EIS was performed in a temperature range of 10°C–60°C to determine the ionic conductivity and activation energy for conduction. The Nyquist plots exhibit only a capacitive tail, indicative of high ionic conductivity, as illustrated in Figures 2A and S4. As depicted in Figure 2B, the temperature dependence of the ionic conductivity follows a linear Arrhenius behavior. Figure 2C illustrates the activation energy for the different samples. Among them, $Li_{5.3}P_{4.3}Cl_{1.7}$ exhibits the highest activation energy of 0.33 eV, followed by $Li_{5.5}PS_{4.5}Cl_{1.5}$ (0.31 eV). Remarkably, the LPSCB SE stands out with the lowest activation energy of 0.27 eV. The ionic conductivities of the as-synthesized lithium argyrodites at 25°C from EIS show an inverse correlation with the activation energy. For $Li_{5.5}PS_{4.5}Cl_{1.5}$, the ionic conductivity is calculated to be 10.6 mS cm^{-1}. Further substituting S with Cl, the ionic conductivity declines to 7.1 mS cm^{-1}, which is most likely due to the presence of LiCl as an impurity in $Li_{5.3}P_{4.3}Cl_{1.7}$. The highest room temperature ionic conductivity of 13.1 mS cm^{-1} is obtained for LPSCB.

To eliminate grain boundary resistance, the LPSCB powder was hot pressed. The resistance of the sintered LPSCB is found to be half that of cold-pressed pellets, corresponding to an ionic conductivity of 25 mS cm^{-1} at 25°C (Figures 2D and S5). Of note, this is one of the highest reported values for sulfide SEs.[9,44] The electronic conductivity of LPSCB from DC polarization measurements was determined to be (3.2 ± 2) × 10^{-13} S cm^{-1} (Figure S6), indicating that the lithium transfer number is close to one.

NMR spectroscopy has been proven to be a suitable probe to gain information about the local structure and the origin of fast ion conduction.[45–47] Well-resolved solid-state ^{6,7}Li and ^{31}P NMR spectra were acquired under MAS of a 10 kHz rate in 3.2 mm rotors. ^{31}P spectra and corresponding simulations are shown in Figures 3A–3C. Three local configurations around the central P atom occupying the four neighboring 4*d* Wyckoff positions (Figure 3A) are observed for $Li_{5.3}PS_{4.3}Cl_{1.7}$, with S_2Cl_2, SCl_3, and Cl_4 at 86, 84, and 82 ppm, respectively.[48] Their occupancies were determined to be 6%, 25%, and 69%, respectively. In the case of $Li_{5.5}PS_{4.5}Cl_{1.5}$, the resonance positions do not alter (Figure 3B); however, the relative occupancies changed to 12%, 38%, and 50%, respectively. For the LPSCB SE, the ^{31}P signals shift to higher frequencies and become broader with indistinct peak intensities (Figure 3C). However, it is difficult to distinguish the contributions from the S^{2-}/Cl^-/Br^- disorder

Please cite this article in press as: Wang et al., Large-scale manufacturing sulfide superionic conductor for advancing all-solid-state batteries, Matter (2025), https://doi.org/10.1016/j.matt.2025.102135

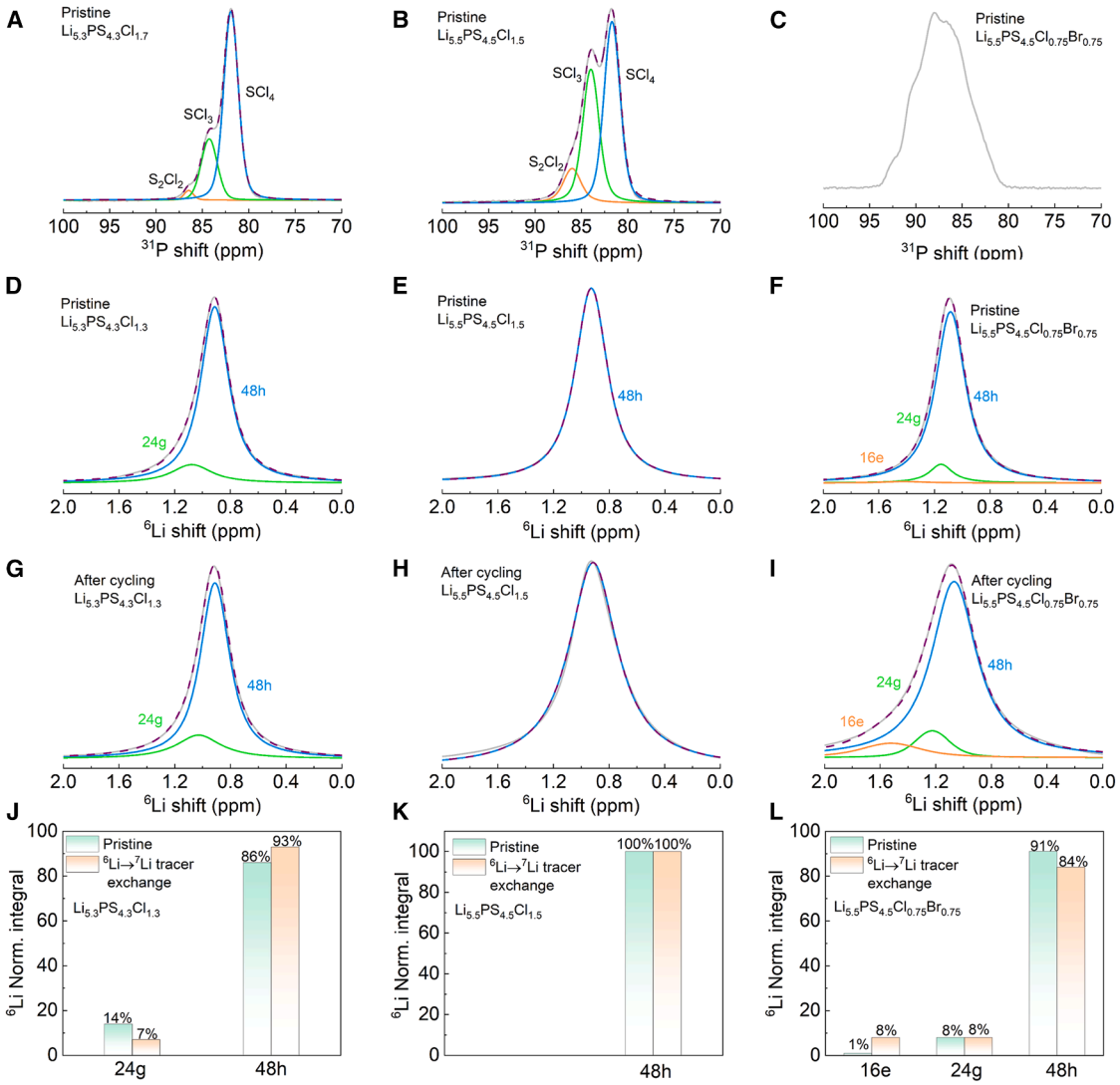

Figure 3. Local structure and ionic transport pathways of lithium argyrodites

Solid-state MAS NMR spectra and corresponding simulations.

(A–F) ^{31}P (A–C) and ^{6}Li (D–F) NMR spectra of the pristine $Li_{5.3}PS_{4.3}Cl_{1.7}$, $Li_{5.5}PS_{4.5}Cl_{1.5}$, and LPSCB SEs, respectively.

(G–I) ^{6}Li NMR spectra of the SEs after $^{6}Li \rightarrow {}^{7}Li$ tracer exchange. The gray curves represent the measured data and the dashed lines in purple are the sum of simulations.

(J–L) Comparisons of Li site fractions in $Li_{5.3}PS_{4.3}Cl_{1.7}$ (J), $Li_{5.5}PS_{4.5}Cl_{1.5}$ (K), and LPSCB (L) SEs before and after $^{6}Li \rightarrow {}^{7}Li$ tracer exchange.

because of 15 possible compositions (e.g., Cl_4, S_4, Br_4, $ClBr_3$, S_2Cl_2, S_3Br, and S_2ClBr) on the four neighboring 4*d* sites. Overall, the broader ^{31}P spectrum of LPSCB indicates a large-degree occupational disorder of anion, leading to enhanced ionic conductivity, which is similar to $Li_{6+x}PS_{5-x}X_{1+x}$ (X = Cl and Br).[16,18,21,27,31] The fundamental reason for the high ionic conductivity of LPSCB needs to be investigated in combination with more in-depth characterization, such as $^{6}Li \rightarrow {}^{7}Li$ tracer-exchange NMR spectroscopy measurements.

Solid-state ^{7}Li NMR spectra of the studied conductors show lower resolution due to strong quadrupolar interactions, as shown in Figure S7. Therefore, we turned to ^{6}Li NMR data of better resolution due to smaller quadrupolar coupling. As shown in Figure 3D, two contributions from the Li sites (24*g* and 48*h*) are clearly observed for the pristine $Li_{5.3}PS_{4.3}Cl_{1.7}$, with relative occupancies of 14% and 86%, respectively. When the Cl content is decreased ($Li_{5.5}PS_{4.5}Cl_{1.5}$), the Li^+ ions solely occupy the 48*h* site (Figure 3E). After additionally introducing Br, a new interstitial Li site (16*e*) is observed, which enables fast intercage movement through 48*h*-16*e*-48*h* pathways, resulting in a higher ionic conductivity (Figure 3F). The occupancies of Li^+ ions on the 16*e*, 24*g*, and 48*h* sites in LPSCB were calculated to be 1%, 8%, and 91% (Table S4), respectively, in good agreement with the results from the NPD analysis. Given the low occupancy of the 16*e* site, it is challenging to detect the lithium with room-temperature NPD. Low-temperature NPD may be more suitable in this case.

However, NMR is sensitive to the local atomic structure, making it an effective method for detecting the 16*e* site.

To probe the Li pathways across the electrolytes, symmetric ^{6}Li|SE|^{6}Li cells were assembled and polarized, and solid-state ^{31}P MAS NMR measurements were carried out afterward. As shown in Figures 3G–3I and S8, the spectra collected after polarization are similar to those of the pristine materials, indicating no structural changes during the measurements. During polarization of the symmetric cells, the ^{6}Li atoms will replace the ^{7}Li and/or ^{6}Li on their way. Figures 3J–3L show a comparison of Li-site fractions for the three SEs before and after ^{6}Li → ^{7}Li tracer exchange. For $Li_{5.3}PS_{4.3}Cl_{1.7}$, the occupancy of ^{6}Li on 48*h* increased from 86% to 93% after polarization (Figure 3J), indicating that it acts as a transition site, enabling fast lithium conduction. In the case of $Li_{5.5}PS_{4.5}Cl_{1.5}$, the amount of ^{6}Li on 48*h* is enriched after tracer exchange (Figure 3K), again suggesting that the 48*h* sites are frequently visited by Li^+ in ion conduction and that they play a pivotal role in long-range migration. However, as mentioned previously, introducing Br alters the lithium substructure and migration pathways. After polarization, the occupancies of Li^+ ions on the 16*e*, 24*g*, and 48*h* sites in LPSCB were determined to be 8%, 8%, and 84%, respectively (Figure 3L). As already suggested, various jump processes contribute to lithium movement, including intra-cage jumps, doublet jumps (within cages), and intercage jumps (between cages). Among these, intercage jumps play a predominant role by providing a shorter route for lithium movement between the cages.[49] The redistribution of the proportion indicates that both 48*h* and 16*e* are involved in migration during the electrochemical cycling. It is obvious that the Li^+ ions frequently migrate through the 16*e* sites via 48*h*-16*e*-48*h* pathways, promoting facile intercage mobility. In contrast to $Li_{5.5}PS_{4.5}Cl_{1.5}$ and $Li_{5.3}PS_{4.3}Cl_{1.7}$, the interstitial 16*e* site in LPSCB is found to also play an important role in achieving higher ionic conductivity. Collectively, we can state that the Li^+ migration pathways in halogen-rich, argyrodite SEs can be tailored by varying the anion composition, as clearly confirmed by ^{6}Li → ^{7}Li tracer-exchange measurements on the atomic level.

To explore the electrochemical performance of the halogen-rich, argyrodite SEs, ASSBs with s-NCM83(coated) as the CAM and In/InLi as the anode were assembled to explore the electrochemical performance of SEs. The cells were cycled in a potential range of 2.2–3.65 V vs. In/InLi, corresponding to 2.8–4.25 V vs. Li^+/Li at room temperature. The composite cathodes consist of 70 wt % s-NCM83(coated) and 30 wt % SE. Figures 4A and S9A show the long-term cycling performance of In/InLi|$Li_{5.5}PS_{4.5}Cl_{1.5}$|s-NCM83(coated)-$Li_{5.5}PS_{4.5}Cl_{1.5}$ cells with an areal loading of 7.1 mg_{CAM} cm^{-2} at room temperature. The cells delivered first-cycle specific charge and discharge capacities of 218 and 177 mAh g^{-1}, respectively, at 0.1 C, resulting in a coulomb efficiency of 81.1%. After some initial cycles, the coulomb efficiency increased to over 99.5%, indicating the highly reversible cycling of the s-NCM83(coated) CAM with minor detrimental side reactions (SE degradation). The specific capacity stabilized at 180 mAh g^{-1} after 100 cycles at 0.1 C. Subsequently, upon increasing the C rate to 1 C, the reversible specific capacity decreased to 116 mAh g^{-1}. However, the cells displayed a high capacity retention of 96% at 1 C, maintaining a specific capacity of 112 mAh g^{-1} after 7,500 cycles with a high average coulomb efficiency of ~99.98%.

The LPSCB ASSBs also exhibited good rate performance and long-term cycling performance. As shown in Figures 4B and 4C, the cells delivered initial specific charge and discharge capacities of 227 and 183 mAh g^{-1}, respectively, at 0.1 C, corresponding to an initial coulomb efficiency of 81%. With an increasing C rate, they delivered specific discharge capacities of 167, 146, 129, and 103 mAh g^{-1} at 0.2, 0.5, 1, and 2 C, respectively. Upon returning to 0.1 C, a specific capacity of 184 mAh g^{-1} was achieved, corresponding to a capacity retention of 100.5% compared to the first cycle, thus demonstrating excellent rate capability and stability. After the C rate increased to 0.5 C in the 32nd cycle, the specific capacity initially declined to 140 mAh g^{-1}, then increased, and finally stabilized around 152 mAh g^{-1} after 2,500 cycles, as shown in Figure 4D. The voltage profiles of the LPSCB cells at different cycles (0.5 C) are depicted in Figure 4E. Good overlap between the 1,000th and 2,500th charge/discharge curves further demonstrates high capacity retention during long-term cycling. Such superior cycling performance surpasses that of most previously reported ASSBs using coated NCM CAMs paired with sulfide SEs. Minor capacity fluctuations are due to temperature variations and/or a sudden power outage in the laboratory.

To showcase the excellent cycle life of the ASSBs at high current densities, cells containing the LPSCB SE were cycled at a high rate of 2 C (3.13 mA cm^{-2}). As shown in Figures 4F and S9B, they delivered a specific discharge capacity of 122 mAh g^{-1} without any notable capacity fading after 1,800 cycles. It should be noted that the areal loading of the above-described cells was 7–8 mg_{CAM} cm^{-2}. Increasing the loading is beneficial for achieving higher areal capacities comparable to those of commercial lithium-ion batteries. Figures 4G and S9C show the cycling performance of a cell with a high CAM loading of 21.4 mg cm^{-2}. As is evident, it delivered, in fact, a stable areal capacity of 2.8 mAh cm^{-2} at room temperature and a 0.1 C rate for 440 cycles.

To monitor the evolution in interfacial resistance, EIS spectra were collected from both the $Li_{5.5}PS_{4.5}Cl_{1.5}$ and LPSCB cells before and after cycling. The corresponding Nyquist plots are shown in Figures 5A and S10. The total impedance of the cell was deconvoluted into the bulk resistance of SE (R_b), the grain boundary resistance of SE (R_{gb}) in the composite cathode, and the s-NCM83|SE ($R_{NCM83|SE}$) and InLi|SE ($R_{InLi|SE}$) interfacial resistances by fitting the spectra using the equivalent circuit depicted in Figure 6A. For the cells containing $Li_{5.5}PS_{4.5}Cl_{1.5}$, the interfacial resistance between the CAM and SE changed notably in comparison with the anode side. The R_b decreased slightly from 23 to 15 Ω after 7,540 cycles, while the $R_{NCM83|SE}$ increased from 7.7 to 43.9 Ω, still allowing for good long-term performance. By contrast, for the cells containing LPSCB, the R_b, R_{gb}, $R_{NCM83|SE}$, and $R_{InLi|SE}$ were found to be lower after 440 cycles. This can be attributed to the densification of the cathode and separator and the formation of a kinetically stable CAM|SE interface, with the latter ensuring stable cycling of even high-loading ASSBs.

Ex situ XPS measurements were further conducted on the LPSCB SE and the composite cathodes at various states of charge. Detail spectra of the S 2p, P 2p, Cl 2p, and Br 3 days

Please cite this article in press as: Wang et al., Large-scale manufacturing sulfide superionic conductor for advancing all-solid-state batteries, Matter (2025), https://doi.org/10.1016/j.matt.2025.102135

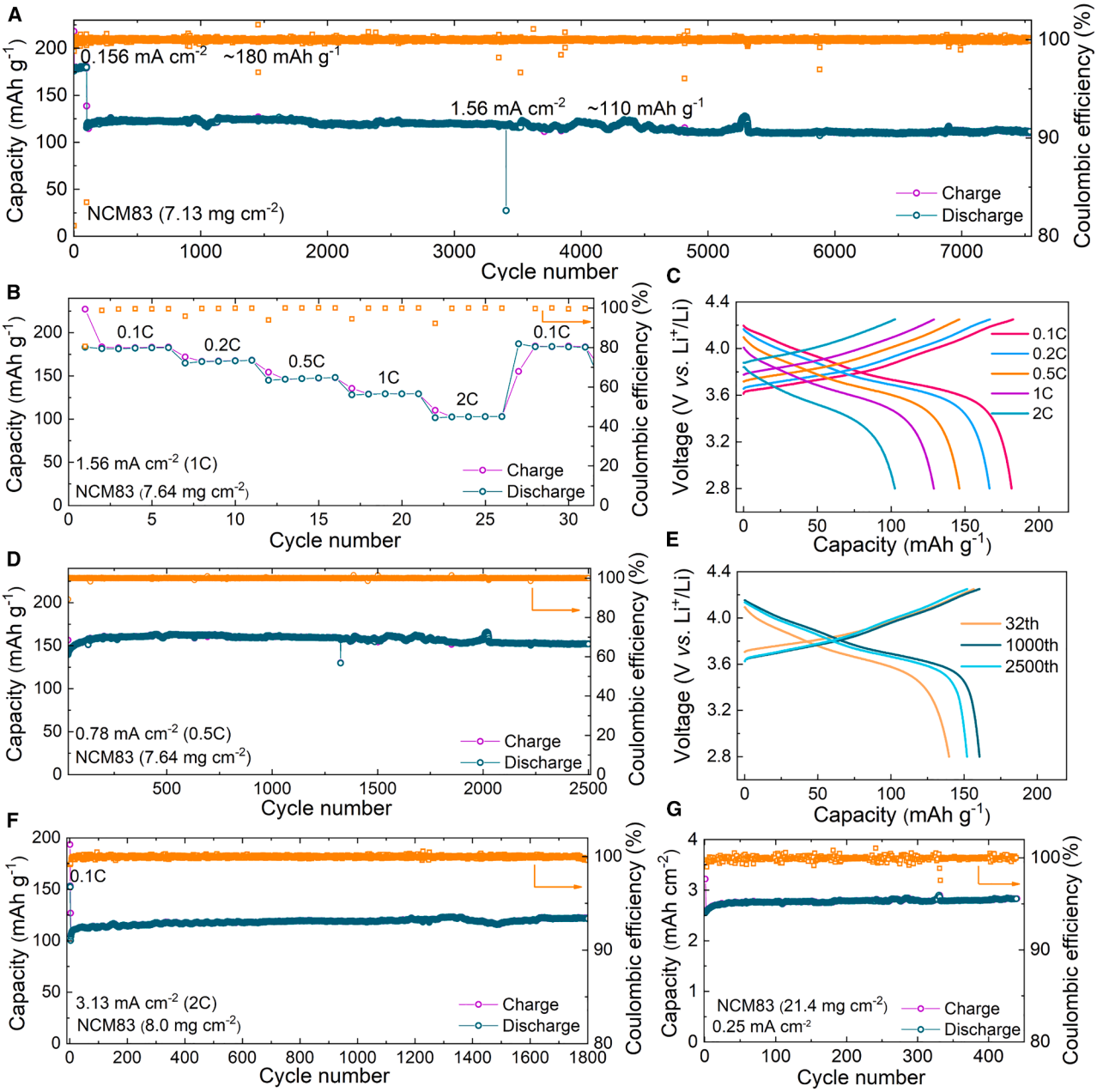

Figure 4. Electrochemical performance of the ASSBs

(A) Cycling performance of an In/InLi|$Li_{5.5}PS_{4.5}Cl_{1.5}$|s-NCM83-$Li_{5.5}PS_{4.5}Cl_{1.5}$ cell at 0.156 mA cm^{-2} over the first 100 cycles and at 1.56 mA cm^{-2} for the following cycles.

(B and D) Rate capability (B) and following cycling performance (D) at 0.78 mA cm^{-2} of an In/InLi|LPSCB|s-NCM83-LPSCB cell.

(C and E) Corresponding voltage profiles for various cycles.

(F and G) Cycling performance of LPSCB cells at a high C rate (3.13 mA cm^{-2}) and with 8.0 mg_{CAM} cm^{-2} areal loading (F) and at a high CAM loading of 21.4 mg cm^{-2} (0.25 mA cm^{-2}) (G).

regions are shown in Figures 5B, 5C, and S11. For LPSCB, the contributions centered at 161.4 eV in the S 2p spectrum and at 131.9 eV in the P 2p spectrum can be assigned to the PS_4^{3-} in the argyrodite phase.[46] The S 2p and P 2p data were unchanged after blending the LPSCB with the s-NCM83 CAM, suggesting that LPSCB SEs do not decompose during mixing. During the first charge to 4.25 V vs. Li^+/Li, the PS_4^{3-} signals decrease, while contributions related to the formation of S_x, P–S–P, and Li_3PO_4 species appear, indicative of interfacial side reactions.[50] The appearance of signals located at higher binding energies is typically attributed to the formation of various thiophosphate species, such as $P_2S_7^{4-}$, $P_2S_6^{2-}$, $P_2S_6^{4-}$, and polysulfides. Apart

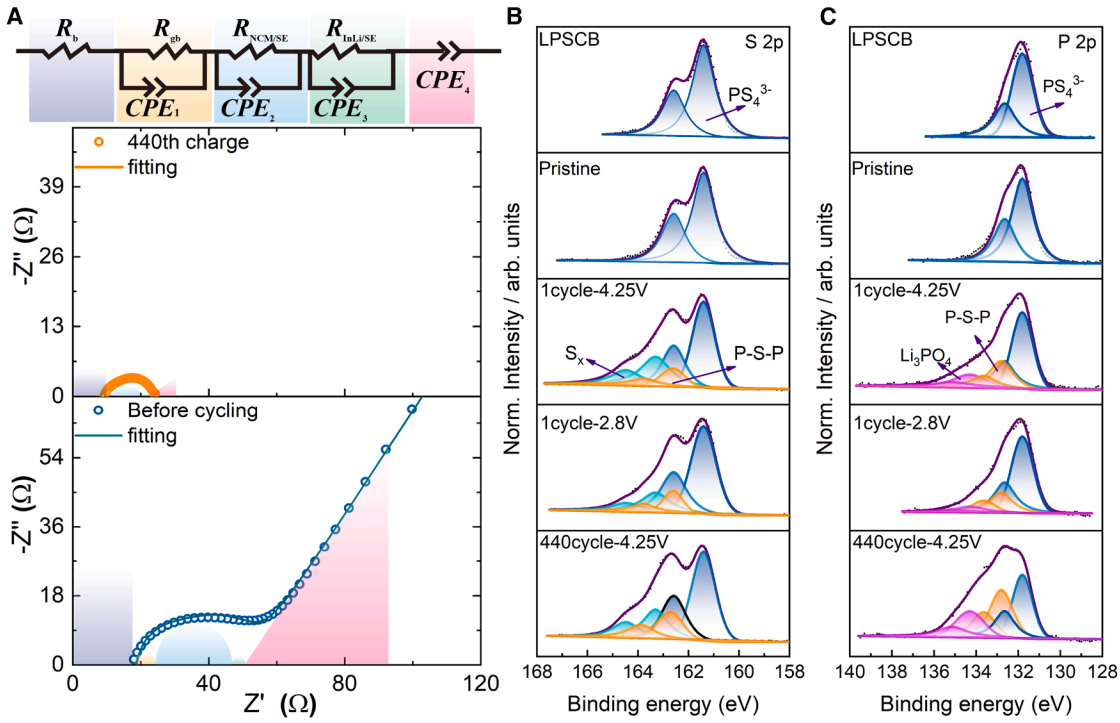

Figure 5. Electrochemical reversibility of NCM83-LPSCB interface using EIS and XPS analysis

(A) Nyquist plots together with the equivalent circuit of In/InLi|LPSCB|sNCM83-LPSCB cells before cycling and after the 440th charge and corresponding fitting plots.

(B and C) XPS spectra of the S 2p (B) and P 2p (C) core levels for pristine and cycled composite cathodes using LPSCB after surface cleaning.

from that, it is difficult to identify the existence of LiCl and LiBr, which might originate from the interfacial decomposition of LPSCB, due to minimal binding energy differences between the Cl (Br) in LiCl (LiBr) and LPSCB (Figure S12).[46] Upon discharging the cell to 2.8 V vs. Li^+/Li, the signals related to S_x and Li_3PO_4 decrease slightly, pointing toward partially reversible degradation of the argyrodite SE. The S_x, P–S–P, and PS_4^{3-} contributions in the S 2p data remained almost unaltered after 440 cycles (relative to the charged state in the initial cycle), and the Li_3PO_4 contribution slightly increased, thus indicating suppressed interfacial reactions between the s-NCM83 CAM and the LPSCB SE. This, in turn, helps explain the superior cycling performance and high capacity retention of ASSB cells using LPSCB.

Conclusions

In summary, we have successfully prepared the superionic conductor LPSCB by altering the degree of anion disorder (S^{2-}/X^-) via halogen mixing. LPSCB exhibits high room temperature ionic conductivities of 13 mS cm^{-1} in the cold-pressed state and 25 mS cm^{-1} after sintering, together with a low activation energy of 0.24 eV. Using fast dry mixing followed by annealing, the preparation of LPSCB at the level of 1 kg per batch is achieved for the first time. In addition, the origin of fast Li^+ migration in the material is revealed through combined EIS, NPD, MAS NMR, and ^6Li-^7Li tracer-exchange NMR spectroscopy measurements. A former overlooked partially occupied 16*e* site in LPSCB is more frequently accessed by Li^+ via 48*h*-16*e*-48*h* intercage jump processes, enabling faster ion conduction in comparison to $Li_{5.5}PS_{4.5}Cl_{1.5}$ and $Li_{5.3}PS_{4.3}Cl_{1.7}$.

Finally, ASSBs with s-NCM83 as the CAM, LPSCB as the electrolyte, and In/InLi as the anode are found to exhibit a remarkable electrochemical performance, displaying superior rate capability and long-term stability (over 2,500 cycles at 0.5 C and 1,800 cycles at 2 C with virtually no capacity fading). Furthermore, the cells are capable of delivering a high areal capacity of 2.8 mAh cm^{-2} after 440 cycles. Such excellent cycling performance is due to the formation of a kinetically stable interface between s-NCM83 and LPSCB, as evidenced by *ex situ* XPS and EIS measurements. Because LPSCB exhibits very high ionic conductivity, low activation energy, and good electrochemical stability, combined with low raw material costs, compared with most other inorganic SEs, including oxides, other thiophosphates, and halides, it is considered to be one of the most promising candidates to accelerate real-world applications of sulfide-based ASSBs.

METHODS

SE synthesis

The LPSCB, $Li_{5.5}PS_{4.5}Cl_{1.5}$, and $Li_{5.3}PS_{4.3}Cl_{1.7}$ SEs were prepared by solid-state reactions. Li_2S (Wuhan Tianshikefeng New Energy Technology, 99.9%), P_2S_5 (Wuhan Tianshikefeng New Energy Technology, 99%), LiCl (Auhui Hengli New Materials,

Please cite this article in press as: Wang et al., Large-scale manufacturing sulfide superionic conductor for advancing all-solid-state batteries, Matter (2025), https://doi.org/10.1016/j.matt.2025.102135

99.9%), and LiBr (Acros, 99%+) as the starting materials were weighed in a stoichiometric ratio and then mixed using a pulverizer (Fangtai Electric Appliance) at 35,000 rpm for 3 min. The photograph of the pulverizer is shown in Figure S12. Afterward, the mixtures were sealed in a quartz container and annealed at 450°C–500°C for 8 h with a heating rate of 90°C h^{-1} in a furnace in the glovebox. Then, the furnace was cooled down to room temperature, and finally, the products were pulverized into fine powders.

Laboratory XRD

The XRD patterns of the SE samples were collected using a diffractometer (SmartLab SE, Rigaku Corporation) equipped with a Cu-K_α radiation source at a scan rate of 1° min^{-1} over a 2θ range of 10°–90°. The SEs were sealed in an airtight holder covered by a Kapton polyimide film to isolate them from ambient atmosphere.

NPD

A cylindrical vanadium container was filled with approximately 2 g of sample. Measurements were carried out at the PEARL neutron powder diffractometer at TU Delft's research reactor, utilizing a germanium monochromator and a wavelength of 1.667 Å. The diffraction data were analyzed via Rietveld refinement using the FullProf Suite software.[51] An empty vanadium container sealed under identical conditions was used to measure the background contribution.

The instrumental contribution to peak shape broadening was calibrated using the Thompson-Cox-Hastings pseudo-Voigt function, with Al_2O_3 serving as the reference standard. An absorption correction was applied during the refinement process. The background was determined by linear interpolation between selected data points in non-overlapping regions. Initially, the zero shift, lattice parameter, and peak shape parameters were determined by Le Bail fitting. The subsequent Rietveld analysis was conducted via sequential refinement of the scale factor, peak shape parameters, lattice parameters, shared S^{2-}/Cl^-/Br^- occupancies on the 4*a*/4*d* sites, atomic coordinates, individual isotropic atomic displacement parameters, and lithium occupancies. The zero-shift parameter was refined last, and any positions yielding unreasonable occupancy or displacement factors were excluded. Finally, all parameters were refined simultaneously to ensure the stability of the calculated structure.

Raman spectroscopy

Spectra were collected in the wavelength range of 100–800 cm^{-1} using a Raman spectrometer (LabRAM Odyssey, Horiba) with an excitation wavelength of 532 nm. The SE pellets were placed on sample holders inside a glovebox, covered with quartz glass, and sealed airtight with epoxy resin to keep an inert atmosphere during measurements.

XPS

Data for the pristine and cycled cathodes were obtained using an XPS spectrometer (AXIS Supra$^+$, Kratos Analytical) equipped with a monochromatic Al-K_α source ($h\nu$ = 1,486.6 eV) to determine the chemical state of elements. The samples were transferred from the glovebox to the spectrometer without exposure to air. The sample surface was cleaned via Ar^+ sputtering at an acceleration voltage of 2 kV for 300 s. Calibration of the binding energies was accomplished by referencing to the Cl 2p3/2 signal at 198.5 eV.

SEM with EDX spectroscopy

The morphology of the SE particles was probed using field-emission SEM (JSM-7610F) at an acceleration voltage of 5 kV with EDX at 15 kV.

MAS NMR spectroscopy

^{6}Li, ^{7}Li, and ^{31}P MAS NMR experiments were performed on a 9.4 T Bruker MHz spectrometer (AVACE NEO) with Larmor frequencies of 58.8, 155.5, and 162 MHz, respectively. A spinning rate of 10 kHz was used for all measurements. Pulse lengths of 5, 2.2, and 2.0 μs were set for polarizing ^{6}Li, ^{7}Li, and ^{31}P, respectively. Chemical shifts were calibrated to LiCl(l) at 0 ppm for ^{6,7}Li and 85% H_3PO_4(l) at 0 ppm for ^{31}P. All spectra were analyzed and processed using the Topspin software (v.4.1.4) together with simulation using the DMfit software.[52]

^{6}Li-^{7}Li exchange NMR spectroscopy

120 mg of SEs was pressed into pellets of 10 mm diameter at 120 MPa. Symmetric ^{6}Li/SE/^{6}Li cells were assembled by pressing ^{6}Li foils on both sides of the pellets followed by an indium foil. Finally, the cells were pressed at 150 MPa for 2 min. Polarization of the symmetric cells was achieved at a constant current density of 0.1 mA cm^{-2} on a LANHE battery testing system for 10 days at room temperature. After cycling, the ^{6}Li and indium foils were removed, and then the SE pellets were ground into fine powder for solid-state NMR characterization.

Electrochemical measurements

To determine the temperature-dependent ionic conductivity and activation energies, ~120 mg of SEs was placed into a polyether ether ketone (PEEK) cylinder and pressed into pellets of 10 mm diameter at 5 tons. Two stainless-steel rods were attached to the pellets as blocking electrodes. AC impedance measurements were performed using an impedance analyzer (Zahner, Zennium Pro) in the frequency range from 1 MHz to 1 Hz with a 10 mV voltage amplitude. The impedance spectra were collected from 10°C to 60°C with 1 h of temperature equilibration prior to data acquisition. For the ionic conductivity measurements of sintered pellets, 400 mg of the annealed LPSCB SE was compressed at 1 ton in a 10 mm pellet die. The pellets were sintered at 1 ton and 400°C for 5 h. After that, two pieces of indium foil were attached to both sides to ensure good contact, and room temperature EIS measurements were conducted at 150 MPa.

For electronic conductivity measurements by DC polarization, 150 mg of SEs was pressed into 10 mm pellets at 150 MPa using a customized Swagelok cell. Two stainless-steel disks were used as current collectors. Voltages of 0.2, 0.4, 0.6, 0.8, and 1.0 V were applied for 6 h to determine the partial electronic conductivity of SEs.

Electrode preparation, cell assembly, and testing

The sNCM83 coated with Li_3BO_3 (LBO) was provided by BASF Shanshan Battery Materials. The sNCM83@LBO was hand ground with $Li_{5.5}PS_{4.5}Cl_{1.5}$ or LPSCB in a mass ratio of 70:30 for 1 h to obtain the sNCM83@LBO-SE composite cathodes. No carbon was added to alleviate the decomposition of SE. The detailed assembly process is as follows: first, ~80 mg of $Li_{5.5}PS_{4.5}Cl_{1.5}$ or LPSCB was pressed into a pellet at 100 MPa in a 10 mm diameter PEEK cylinder. Then, 8–9 mg of the composite cathodes were uniformly spread on one side of the separator layer and pressed at 30 MPa. Next, an indium foil (9 mm diameter, 100 μm thickness) and a lithium foil (4 mm diameter, 10 μm thickness) were sequentially attached to the other side of the separator and pressed at 100 MPa. Finally, the whole cell was compressed at 150 MPa. Galvanostatic cycling of the ASSBs was performed in a potential range of 2.2–3.65 V vs. In/InLi, corresponding to 2.8–4.25 V vs. Li^+/Li at various current densities and room temperature using a LANHE battery testing system (CT3001A). A stack pressure of ~100 MPa was applied to the cells during cycling. The impedance before and after cycling was measured at room temperature using a ZENNIUM PRO potentiostat in the frequency range of 1 MHz to 10 mHz. The C rate was varied from 0.1 to 2 C, with 1 C = 220 mA g_{sNCM83}^{-1}. All assembly and cycling of the cells were conducted in a glovebox. The *in situ* impedance of the cells was measured using a VMP-3 Biologic potentiostat/galvanostat in the frequency range of 1 MHz to 100 mHz at room temperature.

RESOURCE AVAILABILITY

Lead contact

Further information and requests for resources should be directed to and will be fulfilled by the lead contact, Shuo Wang (shuowang@whut.edu.cn).

Materials availability

All unique/stable reagents generated in this study are available from the lead contact with a completed material transfer agreement.

Data and code availability

All data generated during the study are available from the lead contact upon reasonable request. This study did not generate a code.

ACKNOWLEDGMENTS

C.-W.N. acknowledges the Natural Science Foundation of China (grant no. 52388201). S.W. acknowledges the Natural Science Foundation of China (grant no. 52302305) and the Natural Science Foundation Exploration Program of Wuhan (Morning Light Plan) (grant no. 202401jc0089) and support from the Tong Xiang Advanced New Materials Institute. M.T. acknowledges the Natural Science Foundation of China (grant no. 22090043). J.L. acknowledges the Fonds der Chemischen Industrie (FCI) for financial support. F.S. is grateful to the Federal Ministry of Education and Research (BMBF) for funding within the project MELLi (03XP0447). This research used resources at the PEARL neutron source, Delft University of Technology. The authors thank Dr. Xinxin Tan for providing the s-NCM83 cathode material, Yahao Mu for conducting the Raman measurements, and Dr. Indu Dhiman for assistance with the NPD measurements.

AUTHOR CONTRIBUTIONS

S.W. designed the experiments and conducted the main experiments and analyses. C.L. carried out the NMR measurements, and M.T. analyzed the results. X.W. carried out the SEM and XPS measurements. S.L., J.H., and S. W. prepared the SE samples. A.G., Z.C., and S.Z. conducted the NPD measurements, and J.L. and F.S. analyzed the data. S.W., C.L., J.L., F.S., T.B., M.T., and C.-W.N. wrote the manuscript. All authors discussed the results and contributed to the preparation of the manuscript.

DECLARATION OF INTERESTS

The authors declare no competing interests.

SUPPLEMENTAL INFORMATION

Supplemental information can be found online at https://doi.org/10.1016/j.matt.2025.102135.

Received: December 30, 2024
Revised: March 3, 2025
Accepted: April 3, 2025
Published: April 24, 2025

REFERENCES

1. Janek, J., and Zeier, W.G. (2023). Challenges in speeding up solid-state battery development. Nat. Energy *8*, 230–240. https://doi.org/10.1038/s41560-023-01208-9.
2. Cui, G. (2020). Reasonable design of high-energy-density solid-state lithium-metal batteries. Matter *2*, 805–815. https://doi.org/10.1016/j.matt.2020.02.003.
3. Bai, X. (2021). All-solid-state lithium batteries with long cycle life. Matter *4*, 3797–3799. https://doi.org/10.1016/j.matt.2021.11.010.
4. Zhang, Q., Soham, D., Liang, Z., and Wan, J. (2025). Advances in wearable energy storage and harvesting systems. Med-X *3*, 3. https://doi.org/10.1007/s44258-024-00048-w.
5. Zhao, S., Chen, S., Zhou, J., Li, C., Tang, T., Harris, S.J., Liu, Y., Wan, J., and Li, X. (2024). Potential to transform words to watts with large language models in battery research. Cell Rep. Phys. Sci. *5*, 101844. https://doi.org/10.1016/j.xcrp.2024.101844.
6. Guo, N., Chen, S., Tao, J., Liu, Y., Wan, J., and Li, X. (2024). Semi-supervised learning for explainable few-shot battery lifetime prediction. Joule *8*, 1820–1836. https://doi.org/10.1016/j.joule.2024.02.020.
7. Wang, Z.-Y., Zhao, C.-Z., Sun, S., Liu, Y.-K., Wang, Z.-X., Li, S., Zhang, R., Yuan, H., and Huang, J.-Q. (2023). Achieving high-energy and high-safety lithium metal batteries with high-voltage-stable solid electrolytes. Matter *6*, 1096–1124. https://doi.org/10.1016/j.matt.2023.02.012.
8. Dixit, M.B., Singh, N., Horwath, J.P., Shevchenko, P.D., Jones, M., Stach, E.A., Arthur, T.S., and Hatzell, K.B. (2020). In situ investigation of chemo-mechanical effects in thiophosphate solid electrolytes. Matter *3*, 2138–2159. https://doi.org/10.1016/j.matt.2020.09.018.
9. Ohno, S., Banik, A., Dewald, G.F., Kraft, M.A., Krauskopf, T., Minafra, N., Till, P., Weiss, M., and Zeier, W.G. (2020). Materials design of ionic conductors for solid state batteries. Prog. Energy *2*, 022001. https://doi.org/10.1088/2516-1083/ab73dd.
10. Zuo, D., Yang, L., Zou, Z., Li, S., Feng, Y., Harris, S.J., Shi, S., and Wan, J. (2023). Ultrafast synthesis of NASICON solid electrolytes for sodium-metal batteries. Adv. Energy Mater. *13*, 2301540. https://doi.org/10.1002/aenm.202301540.
11. Chen, Y., Wang, T., Chen, H., Kan, W.H., Yin, W., Song, Z., Wang, C., Ma, J., Luo, W., and Huang, Y. (2023). Local structural features of medium-entropy garnet with ultra-long cycle life. Matter *6*, 1530–1541. https://doi.org/10.1016/j.matt.2023.03.002.
12. Hu, Y., Fu, J., Xu, J., Luo, J., Zhao, F., Su, H., Liu, Y., Lin, X., Li, W., Kim, J. T., et al. (2024). Superionic amorphous $NaTaCl_6$ halide electrolyte for highly reversible all-solid-state Na-ion batteries. Matter *7*, 1018–1034. https://doi.org/10.1016/j.matt.2023.12.017.

13. Hatzell, K.B. (2022). Opportunities for halide solid electrolytes in solid-state batteries. Matter *5*, 2533–2535. https://doi.org/10.1016/j.matt.2022.06.055.

14. Feng, Y., Yang, L., Yan, Z., Zuo, D., Zhu, Z., Zeng, L., Zhu, Y., and Wan, J. (2023). Discovery of high entropy garnet solid-state electrolytes via ultrafast synthesis. Energy Storage Mater. *63*, 103053. https://doi.org/10.1016/j.ensm.2023.103053.

15. Wang, S., Zhang, Y., Zhang, X., Liu, T., Lin, Y.H., Shen, Y., Li, L., and Nan, C.W. (2018). High-conductivity argyrodite Li_6PS_5Cl solid electrolytes prepared via optimized sintering processes for all-solid-state lithium-sulfur batteries. ACS Appl. Mater. Interfaces *10*, 42279–42285. https://doi.org/10.1021/acsami.8b15121.

16. Adeli, P., Bazak, J.D., Park, K.H., Kochetkov, I., Huq, A., Goward, G.R., and Nazar, L.F. (2019). Boosting Solid-State Diffusivity and Conductivity in Lithium Superionic Argyrodites by Halide Substitution. Angew. Chem. Int. Ed. *58*, 8681–8686. https://doi.org/10.1002/anie.201814222.

17. Li, S., Lin, J., Schaller, M., Indris, S., Zhang, X., Brezesinski, T., Nan, C.W., Wang, S., and Strauss, F. (2023). High-Entropy Lithium Argyrodite Solid Electrolytes Enabling Stable All-Solid-State Batteries. Angew. Chem. Int. Ed. *62*, e202314155. https://doi.org/10.1002/anie.202314155.

18. Gautam, A., Sadowski, M., Ghidiu, M., Minafra, N., Senyshyn, A., Albe, K., and Zeier, W.G. (2020). Engineering the site-disorder and lithium distribution in the lithium superionic argyrodite Li_6PS_5Br. Adv. Energy Mater. *11*, 2003369. https://doi.org/10.1002/aenm.202003369.

19. de Klerk, N.J.J., Rosłoń, I., and Wagemaker, M. (2016). Diffusion mechanism of Li argyrodite solid electrolytes for Li-Ion batteries and prediction of optimized halogen doping: The effect of Li vacancies, halogens, and halogen disorder. Chem. Mater. *28*, 7955–7963. https://doi.org/10.1021/acs.chemmater.6b03630.

20. Lin, J., Cherkashinin, G., Schäfer, M., Melinte, G., Indris, S., Kondrakov, A., Janek, J., Brezesinski, T., and Strauss, F. (2022). A high-entropy multicationic substituted lithium argyrodite superionic solid electrolyte. ACS Mater. Lett. *4*, 2187–2194. https://doi.org/10.1021/acsmaterialslett.2c00667.

21. Kraft, M.A., Ohno, S., Zinkevich, T., Koerver, R., Culver, S.P., Fuchs, T., Senyshyn, A., Indris, S., Morgan, B.J., and Zeier, W.G. (2018). Inducing high ionic conductivity in the lithium superionic argyrodites $Li_{6+x}P_{1-x}Ge_xS_5I$ for all-solid-state batteries. J. Am. Chem. Soc. *140*, 16330–16339. https://doi.org/10.1021/jacs.8b10282.

22. Zhou, L., Assoud, A., Zhang, Q., Wu, X., and Nazar, L.F. (2019). New family of argyrodite thioantimonate lithium superionic conductors. J. Am. Chem. Soc. *141*, 19002–19013. https://doi.org/10.1021/jacs.9b08357.

23. Kamaya, N., Homma, K., Yamakawa, Y., Hirayama, M., Kanno, R., Yonemura, M., Kamiyama, T., Kato, Y., Hama, S., Kawamoto, K., and Mitsui, A. (2011). A lithium superionic conductor. Nat. Mater. *10*, 682–686. https://doi.org/10.1038/nmat3066.

24. Du, J., Lin, J., Zhang, R., Wang, S., Indris, S., Ehrenberg, H., Kondrakov, A., Brezesinski, T., and Strauss, F. (2024). Electrochemical testing and benchmarking of compositionally complex lithium argyrodite electrolytes for all-solid-state battery application. Batter. Supercaps *7*, e202400112. https://doi.org/10.1002/batt.202400112.

25. Wang, S., Fang, R., Li, Y., Liu, Y., Xin, C., Richter, F.H., and Nan, C.-W. (2021). Interfacial challenges for all-solid-state batteries based on sulfide solid electrolytes. J. Materiomics *7*, 209–218. https://doi.org/10.1016/j.jmat.2020.09.003.

26. Li, S., Yang, Z., Wang, S.-B., Ye, M., He, H., Zhang, X., Nan, C.-W., and Wang, S. (2024). Sulfide-based composite solid electrolyte films for all-solid-state batteries. Commun. Mater. *5*, 44. https://doi.org/10.1038/s43246-024-00482-8.

27. Gautam, A., Ghidiu, M., Suard, E., Kraft, M.A., and Zeier, W.G. (2021). On the lithium distribution in halide superionic argyrodites by halide incorporation in $Li_{7-x}PS_{6-x}Cl_x$. ACS Appl. Energy Mater. *4*, 7309–7315. https://doi.org/10.1021/acsaem.1c01417.

28. Gautam, A., Al-Kutubi, H., Famprikis, T., Ganapathy, S., and Wagemaker, M. (2023). Exploring the relationship between halide substitution, structural disorder, and lithium distribution in lithium argyrodites ($Li_{6-x}PS_{5-x}Br_{1+x}$). Chem. Mater. *35*, 8081–8091. https://doi.org/10.1021/acs.chemmater.3c01525.

29. Subramanian, Y., Rajagopal, R., and Ryu, K.-S. (2022). Synthesis, air stability and electrochemical investigation of lithium superionic bromine substituted argyrodite ($Li_{6-x}PS_{5-x}Cl_{1.0}Br_x$) for all-solid-state lithium batteries. J. Power Sources *520*, 230849. https://doi.org/10.1016/j.jpowsour.2021.230849.

30. Liu, Y., Su, H., Zhong, Y., Zheng, M., Hu, Y., Zhao, F., Kim, J.T., Gao, Y., Luo, J., Lin, X., et al. (2024). Inhibiting dendrites by uniformizing microstructure of superionic lithium argyrodites for all-solid-state lithium metal batteries. Adv. Energy Mater. *14*, 2400783. https://doi.org/10.1002/aenm.202400783.

31. Kraft, M.A., Culver, S.P., Calderon, M., Böcher, F., Krauskopf, T., Senyshyn, A., Dietrich, C., Zevalkink, A., Janek, J., and Zeier, W.G. (2017). Influence of lattice polarizability on the ionic conductivity in the lithium superionic argyrodites Li_6PS_5X (X = Cl, Br, I). J. Am. Chem. Soc. *139*, 10909–10918. https://doi.org/10.1021/jacs.7b06327.

32. Cronau, M., Szabo, M., and Roling, B. (2021). Single-step ball milling synthesis of highly Li^+ conductive $Li_{5.3}PS_{4.3}ClBr_{0.7}$ glass ceramic electrolyte enables low-impedance all-solid-state batteries. Mater. Adv. *2*, 7842–7845. https://doi.org/10.1039/D1MA00784J.

33. Yu, C., Li, Y., Willans, M., Zhao, Y., Adair, K.R., Zhao, F., Li, W., Deng, S., Liang, J., Banis, M.N., et al. (2020). Superionic conductivity in lithium argyrodite solid-state electrolyte by controlled Cl-doping. Nano Energy *69*, 104396. https://doi.org/10.1016/j.nanoen.2019.104396.

34. Zhou, L., Park, K.-H., Sun, X., Lalère, F., Adermann, T., Hartmann, P., and Nazar, L.F. (2018). Solvent-engineered design of argyrodite Li_6PS_5X (X = Cl, Br, I) solid electrolytes with high ionic conductivity. ACS Energy Lett. *4*, 265–270. https://doi.org/10.1021/acsenergylett.8b01997.

35. Wu, L., Zhang, Z., Liu, G., Weng, W., Zhang, Z., and Yao, X. (2021). Wet-milling synthesis of superionic lithium argyrodite electrolytes with different concentrations of lithium vacancy. ACS Appl. Mater. Interfaces *13*, 46644–46649. https://doi.org/10.1021/acsami.1c13031.

36. Zuo, T.T., Walther, F., Teo, J.H., Rueß, R., Wang, Y., Rohnke, M., Schröder, D., Nazar, L.F., and Janek, J. (2023). Impact of the chlorination of lithium argyrodites on the electrolyte/cathode interface in solid-state batteries. Angew. Chem. Int. Ed. *62*, e202213228. https://doi.org/10.1002/anie.202213228.

37. Liang, Y., Liu, H., Wang, G., Wang, C., Ni, Y., Nan, C.W., and Fan, L.Z. (2022). Challenges, interface engineering, and processing strategies toward practical sulfide-based all-solid-state lithium batteries. Inf. Manage. *4*, e12292. https://doi.org/10.1002/inf2.12292.

38. Zhang, J., Fu, J., Lu, P., Hu, G., Xia, S., Zhang, S., Wang, Z., Zhou, Z., Yan, W., Xia, W., et al. (2025). Challenges and strategies of low-pressure all-solid-state batteries. Adv. Mater. *37*, e2413499. https://doi.org/10.1002/adma.202413499.

39. Liu, Y., Su, H., Zhong, Y., Wang, X., Xia, X., Gu, C., and Tu, J. (2022). Revealing the impact of Cl substitution on the crystallization behavior and interfacial stability of superionic lithium argyrodites. Adv. Funct. Mater. *32*, 2207978. https://doi.org/10.1002/adfm.202207978.

40. Zhou, L., Kwok, C.Y., Shyamsunder, A., Zhang, Q., Wu, X., and Nazar, L.F. (2020). A new halospinel superionic conductor for high-voltage all solid state lithium batteries. Energy Environ. Sci. *13*, 2056–2063. https://doi.org/10.1039/D0EE01017K.

41. Ishiguro, Y., Ueno, K., Nishimura, S., Iida, G., and Igarashib, Y. (2023). $TaCl_5$-glassified Ultrafast Lithium Ion-conductive Halide Electrolytes for High-performance All-solid-state Lithium Batteries. Chem. Lett. *52*, 237–241. https://doi.org/10.1246/cl.220540.

42. Li, X., Liang, J., Luo, J., Norouzi Banis, M., Wang, C., Li, W., Deng, S., Yu, C., Zhao, F., Hu, Y., et al. (2019). Air-stable Li_3InCl_6 electrolyte with high

voltage compatibility for all-solid-state batteries. Energy Environ. Sci. *12*, 2665–2671. https://doi.org/10.1039/C9EE02311A.

43. Ren, Y., Deng, H., Chen, R., Shen, Y., Lin, Y., and Nan, C.-W. (2015). Effects of Li source on microstructure and ionic conductivity of Al-contained $Li_{6.75}La_3Zr_{1.75}Ta_{0.25}O_{12}$ ceramics. J. Eur. Ceram. Soc. *35*, 561–572. https://doi.org/10.1016/j.jeurceramsoc.2014.09.007.
44. Li, Y., Song, S., Kim, H., Nomoto, K., Kim, H., Sun, X., Hori, S., Suzuki, K., Matsui, N., Hirayama, M., et al. (2023). A lithium superionic conductor for millimeter-thick battery electrode. Science *381*, 50–53. https://doi.org/10.1126/science.add7138.
45. Zheng, J., Tang, M., and Hu, Y.Y. (2016). Lithium ion pathway within $Li_7La_3Zr_2O_{12}$ -polyethylene oxide composite electrolytes. Angew. Chem. Int. Ed. *55*, 12538–12542. https://doi.org/10.1002/anie.201607539.
46. Wang, S., Tang, M., Zhang, Q., Li, B., Ohno, S., Walther, F., Pan, R., Xu, X., Xin, C., Zhang, W., et al. (2021). Lithium argyrodite as solid electrolyte and cathode precursor for solid-state batteries with long cycle life. Adv. Energy Mater. *11*, 2101370. https://doi.org/10.1002/aenm.202101370.
47. Lou, C., Liu, J., Sun, X., Zhang, W., Xu, L., Luo, H., Chen, Y., Gao, X., Kuang, X., Fu, J., et al. (2024). Correlating local structure and migration dynamics in Na/Li dual ion conductor $Na_5YSi_4O_{12}$. Proc. Natl. Acad. Sci. USA *121*, e2401109121. https://doi.org/10.1073/pnas.2401109121.
48. Feng, X., Chien, P.-H., Wang, Y., Patel, S., Wang, P., Liu, H., Immediato-Scuotto, M., and Hu, Y.-Y. (2020). Enhanced ion conduction by enforcing structural disorder in Li-deficient argyrodites $Li_{6-x}PS_{5-x}Cl_{1+x}$. Energy Storage Mater. *30*, 67–73. https://doi.org/10.1016/j.ensm.2020.04.042.
49. Schwietert, T.K., Gautam, A., Lavrinenko, A.K., Drost, D., Famprikis, T., Wagemaker, M., and Vasileiadis, A. (2024). Understanding the role of aliovalent cation substitution on the li-ion diffusion mechanism in $Li_{6+x}P_{1-x}Si_xS_5Br$ argyrodites. Mater. Adv. *5*, 1952–1959. https://doi.org/10.1039/D3MA01042B.
50. Wang, S., Zhang, W., Chen, X., Das, D., Ruess, R., Gautam, A., Walther, F., Ohno, S., Koerver, R., Zhang, Q., et al. (2021). Influence of crystallinity of lithium thiophosphate solid electrolytes on the performance of solid-state batteries. Adv. Energy Mater. *11*, 2100654. https://doi.org/10.1002/aenm.202100654.
51. Rodríguez-Carvajal, J. (1993). Recent advances in magnetic structure determination by neutron powder diffraction. Physica B *192*, 55–69. https://doi.org/10.1016/0921-4526(93)90108-I.
52. Massiot, D., Fayon, F., Capron, M., King, I., Le Calvé, S., Alonso, B., Durand, J.O., Bujoli, B., Gan, Z., and Hoatson, G. (2001). Modelling one- and two-dimensional solid-state NMR spectra. Magn. Reson. Chem. *40*, 70–76. https://doi.org/10.1002/mrc.984.